ISSN 1674-1056
http://cpb.iphy.ac.cn
http://iopscience.iop.org/cpb
中国物理 B
Chinese Physics
中国物理
Chinese Physics B

Influence of warm eddies on sound propagation in the Gulf of Mexico

Yao Xiao(肖瑶), Zhenglin Li(李整林), Jun Li(李鋆), Jiaqi Liu(刘佳琪), Karim G Sabra

Citation: Chin. Phys. B . 2019, 28(5): 054301. **doi:** 10.1088/1674-1056/28/5/054301
Journal homepage: http://cpb.iphy.ac.cn; http://iopscience.iop.org/cpb

What follows is a list of articles you may be interested in

Effects of rough surface on sound propagation in shallow water

Ruo-Yun Liu(刘若芸), Zheng-Lin Li(李整林)

Chin. Phys. B . 2019, 28(1): 014302. **doi:** 10.1088/1674-1056/28/1/014302

Effect of the fluctuant acoustic channel on the gain of a linear array in the ocean waveguide

Lei Xie(谢磊), Chao Sun(孙超), Guang-Yu Jiang(蒋光禹), Xiong-Hou Liu(刘雄厚), De-Zhi Kong(孔德智)

Chin. Phys. B . 2018, 27(11): 114301. **doi:** 10.1088/1674-1056/27/11/114301

Radiation from finite cylindrical shell with irregular-shaped acoustic enclosure

De-Sen Yang(杨德森), Rui Zhang(张睿), Sheng-Guo Shi(时胜国)

Chin. Phys. B . 2018, 27(10): 104301. **doi:** 10.1088/1674-1056/27/10/104301

Three-dimensional parabolic equation model for seismo-acoustic propagation:Theoretical development and preliminary numerical implementation

Jun Tang(唐骏), Sheng-Chun Piao(朴胜春), Hai-Gang Zhang(张海刚)

Chin. Phys. B . 2017, 26(11): 114301. **doi:** 10.1088/1674-1056/26/11/114301

Developments of parabolic equation method in the period of 2000-2016

Chuan-Xiu Xu(徐传秀), Jun Tang(唐骏), Sheng-Chun Piao(朴胜春), Jia-Qi Liu(刘佳琪), Shi-Zhao Zhang(张士钊)

Chin. Phys. B . 2016, 25(12): 124315. **doi:** 10.1088/1674-1056/25/12/124315

Influence of warm eddies on sound propagation in the Gulf of Mexico*

Yao Xiao(肖瑶)[1,2], Zhenglin Li(李整林)[1,†], Jun Li(李鋆)[3], Jiaqi Liu(刘佳琪)[4], and Karim G Sabra[5]

[1] State Key Laboratory of Acoustics, Institute of Acoustics, Chinese Academy of Sciences, Beijing 100190, China
[2] University of Chinese Academy of Sciences, Beijing 100049, China
[3] China State Shipbuilding Corporation (CSSC) Systems Engineering Research Institute, Beijing 100049, China
[4] College of Underwater Acoustic Engineering, Harbin Engineering University, Harbin 150001, China
[5] Woodruff School Mechanical Engineering, Georgia Institute of Technology, 771 Ferst Drive NW, Atlanta, Georgia 30332-0405, USA

(Received 28 January 2019; revised manuscript received 22 February 2019; published online 20 March 2019)

An automatic detection method is employed to identify and track eddies in the Gulf of Mexico. The physical parameters of the eddies, such as lifespan, radius, and distribution position are first examined and used to determine the spatio–temporal evolution of a strong warm eddy separated from the Mexico current. Then, the influence of this strong warm eddy on sound propagation during its lifespan are comprehensively analyzed with the parabolic equation and explained by using the normal mode and ray theories. Additionally, the influence of mesoscale eddies on the redistribution of total depth-integrated energy among the normal modes in the deep water is also discussed. The variation of arrival angle is investigated to explain the spreading acoustic energy caused by eddies. Overall, the results show that warm eddies can change the propagation paths and cause the convergence zone to broaden and approach the sound source. Moreover, the warm eddy can disperse sound energy and cause the total depth-integrated energy to incline to a lower normal mode. Throughout the whole of these three periods (eddy generating, eddy maturing, and eddy terminating), the fluctuation in the transmission loss is up to 30 dB (depending on the relative location of eddy center to the source).

Keywords: mesoscale eddies, sound propagation, mode coupling, acoustic energy disturbance

PACS: 43.30.+m, 43.30.Bp, 43.30.Cq, 92.10.Vz **DOI:** 10.1088/1674-1056/28/5/054301

1. Introduction

Mesoscale eddies, similar to cyclones or storms in the atmosphere,[1–4] are relatively large coherent rotating bodies of water in the ocean. They are often accompanied by large ocean currents. For instance, at the edge of the Kuroshio, there are usually mesoscale eddies with radii of tens to hundreds of kilometers. According to previous studies,[1–7] eddies move slowly and can thus be considered as the quasi-static feature in the water column when compared to the much faster time-scale of sound propagation. Since the cold or warm water carried by mesoscale eddies can significantly change the ocean temperature and salinity distribution, mesoscale eddies can significantly change the sound speed profile structure, thus affecting underwater sound propagation. Consequently, it is meaningful for oceanographers and acousticians to understand the influence of mesoscale eddies on acoustic propagation, which has a broad application in the inversion of sound field environment, the underwater communication, the detection of ocean information, and so on.

Several studies have investigated the physical characteristics of mesoscale eddies and their influence on long-range sound transmission.[5–13] Henrick presented an analysis of the influence of mesoscale eddies on sound propagation and the received time-series which were solved by the ray-mode theory algorithm.[6,7] Hall used adiabatic normal mode model to compute the horizontal refraction of the acoustic signal caused by mesoscale eddies.[8] The effects of cold-core eddies on the propagation of Sound Fixing and Ranging (SOFAR) channels were studied by Vastano and Owens[9] using numerical simulation based on geometric acoustics theory for a source that was located at the center of an eddy. Weinberg and Zabalgogeazcoa then discussed sound sources located outside the eddy.[10] Bare[11] studied the horizontal and vertical refraction of the sound propagation characteristics in the eddy area using three-dimensional parabolic equation model. Because of the seasonal distribution of mesoscale eddies, Lawrence studied the effects of eddy on sound propagation in winter and summer.[12] Chen[14] revealed the influence mechanism of eddies on acoustic propagation from the perspective of surface waveguide by using the Array for Real-Time Geostrophic Oceanography (ARGO) buoy data and typical two-dimensional (2D) ray algorithm. Heaney[15] used a fully three-dimensional parabolic equation model to examine the horizontal refraction due to mesoscale eddy at low frequency acoustics in the South Indian Ocean.

Generally, the influence of eddies on sound propagation is investigated using modelled eddy geometry.[5–13] However,

*Project supported by the National Natural Science Foundation of China (Grant Nos. 11434012 and 41561144006).
†Corresponding author. E-mail: lzhl@mail.ioa.ac.cn
© 2019 Chinese Physical Society and IOP Publishing Ltd

the method using traditional acoustic propagation analysis method combined with the ideal eddy to examine the influence of the mesoscale eddy on the sound propagation cannot meet the actual applications. Furthermore, the physical characteristics of the real eddies and the influence of acoustic energy fluctuation during their whole lifespan are not systematically examined and analyzed. Therefore, it becomes increasingly important to use a data assimilation procedure that assimilates the actual physical properties of the eddies, in combination with typical and newest research method to analyze and explain the sound filed fluctuation throughout the different periods of actual eddies in the real ocean environment. In this paper, an automatic detection method for eddy[16] combined with the satellite data and oceanography assimilation data is used to identify and track regional eddies in the Gulf of Mexico throughout their lifespan; i.e., including the evolution of their radius and spatial distribution. In particular, the influences on sound propagation of a strong warm eddy, identified with this automated procedure, are comprehensively examined during the whole lifespan of the eddy and systematically analyzed. Additionally, the normal mode and ray theories, the total depth-integrated energy and single mode as initial field method, and the receiving arrival angle are all used to explain and understand the effect of warm eddies on acoustic propagation, such as energy deflection and mode coupling.

The rest of this article is organized as follows. Section 2 presents the statistics of eddies in the Gulf of Mexico to determine realistic environmental parameters for the subsequent numerical. Section 3 extracts a strong eddy shedding from the Gulf of Mexico current and analyzes its effect on sound propagation. Section 4 examines the acoustic energy fluctuations during the lifespan of the eddy. Finally, Section 5 summarizes the results and conclusions drawn from this study.

2. Eddy statistics in the Gulf of Mexico

To study the effects of eddy on sound propagation, the characteristic parameters of the eddies in the Mexico Gulf are analyzed using the satellite remote sensing data from Copernicus Marine Environment Monitoring Service (CMEMS).[17] Specifically, we use the SEALEVEL_GLO_PHY L4_NRT_OBSERVATIONS_008_046 dataset. An eddy automatic detection method[16] is used to identify and track the eddies in the Gulf Stream region. The lifespan, radius, and distribution position of the eddies are examined from 1993 to 2014. The principle of this detection method is: (i) the sea level anomaly (SLA) is an enclosed curve; (ii) the depth needs to exceed 800 m at the center of the eddy; (iii) the height difference between the eddy center and the outermost layer of the closed contour is no less than 5 cm; (iv) the eddies can be traced for at least 20 days under the conditions of the first three criteria. The tracks of these eddies are identified every seven days, but only the eddies with a radius greater than 20 km are retrained for statistical analysis. Moreover, the spatial distribution of eddies is present by the number of eddies' center at each pixel from 1993 to 2014.

The results show that the detected number of cyclone eddies (cold) and anti-cyclone (warm) eddies are 3191 and 3004,

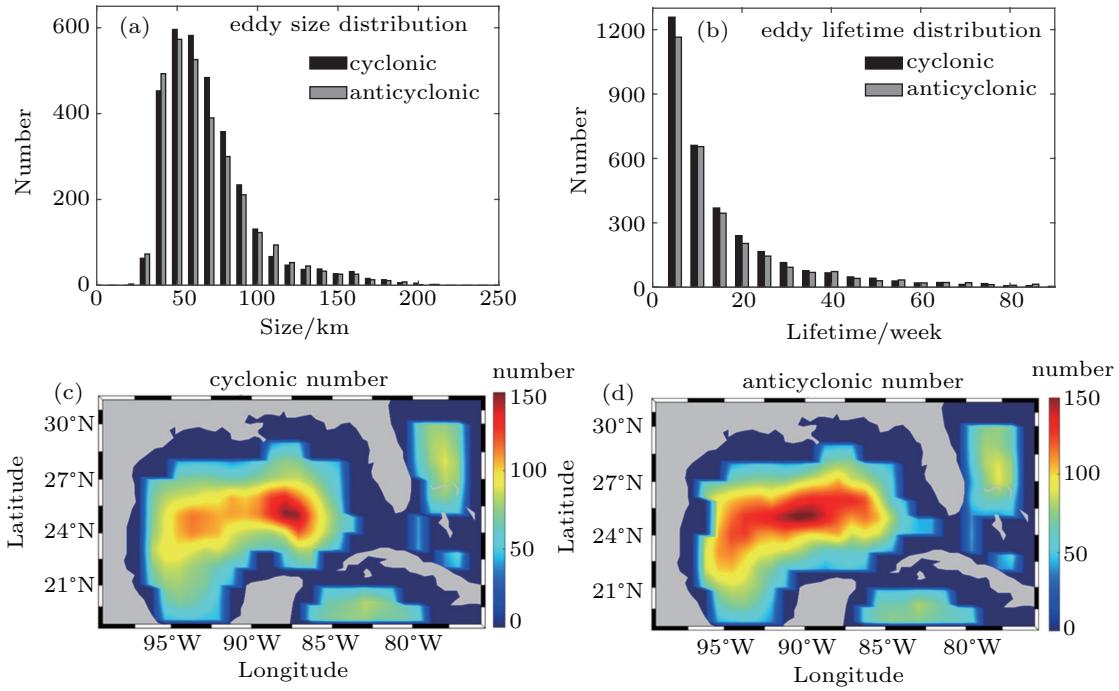


Fig. 1. Statistics of the Gulf Stream eddies of 20 years from 1993 to 2014. (a) Histograms of the eddy size. Black color indicates cyclonic eddies, while the gray color indicates anticyclonic eddies. (b) Histograms of the eddy lifetimes. (c) The spatial distribution of the site associated with the vertical color scale indicates the number of eddies' center at each pixel. (d) Same as (c), but for anticyclonic eddies.

respectively. The histogram of radius distribution (Fig. 1(a)) presents that the radius of eddies in the Gulf of Mexico can be approximately characterized by a normal distribution. The average radius of the eddy is 55 km. The average radius of the cyclone eddy and the anti-cyclonic eddy is 56 km and 54 km respectively. Eddies with a radius of 40–100 km account for 90% of the total, while eddies with a radius more than 200 km account for only 0.3% of the total. Figure 1(b) shows that the lifespan of eddies varies from a few weeks to several months. The average lifetime can be 8 weeks and 82% of eddies can even exist for 20 weeks, with the longest being up to 90 weeks. However, less than 2% can last for more than one year. Figures 1(c) and 1(d) show the eddies distribution in the Gulf of Mexico and the characteristics of the westward movements of eddies, which meets the feature of Rossby wave and the direction of ground flow. As the large upslope in continental shelf accelerates the decay of eddies, the eddies' distribution is in line with the bathymetry trends along the deeper region. Furthermore, anticyclonic (warm) eddies incline to propagate farther due to the high energy from the current.

3. Quantifying the influences of a strong eddy on sound propagation

To better capture the marine environment for calculating the effect of mesoscale eddy on sound propagation, the profiles of the temperature T and salinity S obtained from the Global Ocean Reanalysis[18] are used to compute the effective sound speed profile. This product is a reanalysis of the ocean state obtained by constraining the nucleus for European modelling of the ocean model at 1/4° resolution with *in situ* T and S profiles including ARGO and Marine Mammals Exploring the Oceans Pole to Pole (MEOP) profiles, the satellite sea surface temperature, and along-track sea level anomalies. In this section, a strong eddy is picked up in the region of [85°W–92°W, 24.5°N–28°N] on September 26, 2014, as shown in Figs. 2(a) and 2(b). This eddy is separated from the current of the Gulf of Mexico. The maximum surface velocity of the eddy reaches 168.8 cm/s, and the maximum surface sound speed is 1534.1 m/s. The center of the eddy is located at 88.1667°W, 27.1667°N along with the vertical center at a depth of 244.9 m. Figure 2(b) shows that the radius of the closed loop of the eddy is about 135.6 km. Figure 2(c) presents the sound speed horizontally and vertically affected area reaching up to 500 km and 1700 m, respectively. The distribution of sound speed is shown in Figs. 2(c) and 2(d). The dashed red line in Fig. 2(c) shows the bathymetry along the red line in Fig. 2(b). The maximum water depth reaches 3138.6 m and the average depth is 2600 m. The thick red line in Fig. 2(d) indicates the background sound speed profile, which is obtained by averaging the data from 1993–2014 in the Gulf of Mexico. It can be seen that the sound speed has been disturbed due to the existence of the warm eddies. The maximum fluctuation of the sound speed amounts to 32.7 m/s, which in turn affects the sound transmission.

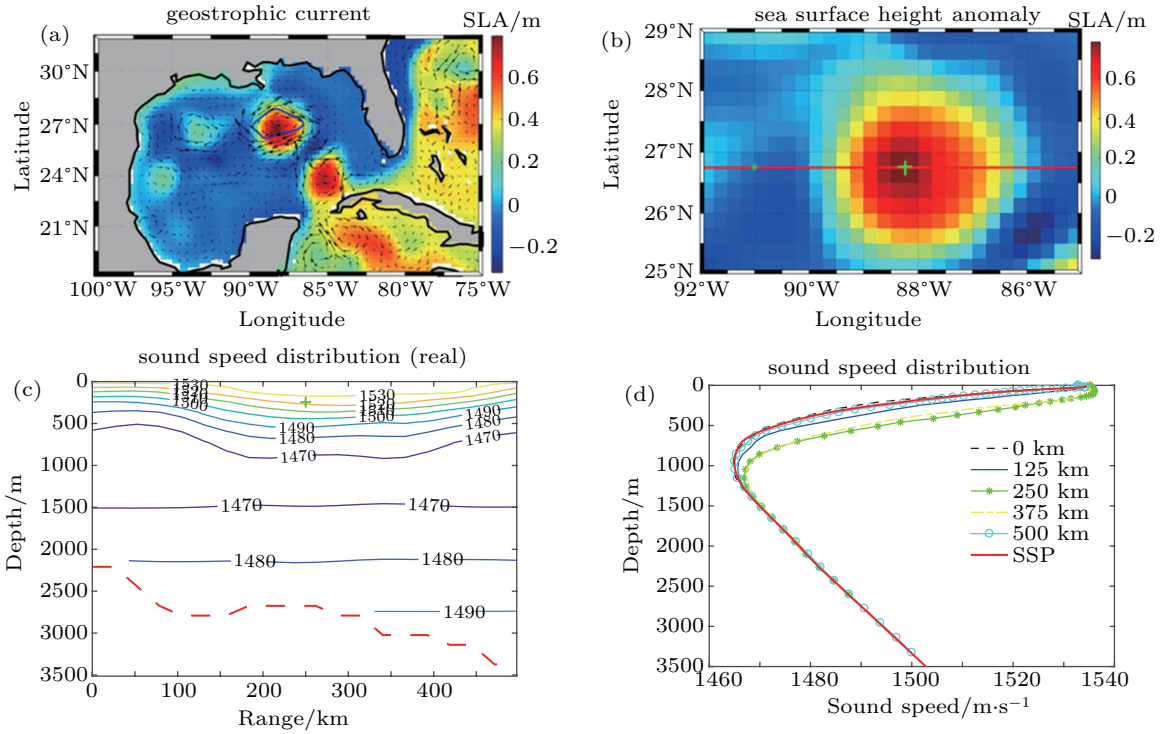


Fig. 2. The ocean environment parameter of the Gulf of Mexico with the presence of a strong eddy. (a) Surface velocity field and sea level anomaly (SLA) on September 26, 2014. The solid lines indicate the eddy boundaries. The color scale indicates the SLA in m. (b) SLA of the region is shown and magnified. The green cross indicates the horizontal location of eddy center. (c) Sound speed displacement contour along the red line in Fig. 2(b). The contour line indicates the sound speed in m/s. The green cross indicates the vertical location of eddy center. (d) Sound speed profiles (SSPs) at different ranges from the source.

The ocean environment in Fig. 2(c) is employed to simulate the effects of eddy on sound propagation in this section. The geoacoustic parameters shown in Table 1 are used in the acoustic propagation simulation, which are extracted from the Gulf of Mexico geological and geophysical (G&G) activities draft programmatic environmental impact statement (EIS) (see Appendix D, Table D-3 of Ref. [19]). The source is located at the depth of 300 m and the central frequency is 160 Hz. The parabolic equation (PE) model RAM-PE[20,21] is used to calculate the range dependent sound field. The sound pressure form of the solution by using Padé approximation is as follows:

$$p(r+\Delta r,z)=\exp(\mathrm{i}k_0\Delta r)\prod_{j=1}^{n}\frac{1+\alpha_{j,n}X}{1+\beta_{j,n}X}p(r,z), \quad (1)$$

$$X=k_0^{-2}(\rho\frac{\partial}{\partial z}\frac{1}{\rho}\frac{\partial}{\partial z}+k^2-k_0^2), \quad (2)$$

where $k_0=w/c_0$ and c_0 is a representative phase speed, $k=(1+\mathrm{i}\eta\beta)w/c$ is the wave number, ρ is the density, w is the circular frequency, c is the speed of sound, β is the attenuation in $\mathrm{d}B/\lambda$, and $\eta=(40\pi\log_{10}\mathrm{e})^{-1}$. Δr is the range step, $\alpha_{j,n}$ and $\beta_{j,n}$ are Padé coefficients. The Galerkin discrete[21] formula is used to discretize the equation above into a matrix. According to the sound pressure at range r, the field at range $r+\Delta r$ can be obtained, which has high accuracy for middle and low frequencies and long distances.[22] The background sound speed shown by the red line in Fig. 2(d) is used as the reference environment without eddy.

Figure 3 shows a comparison of transmission loss (TL) in the Mexico Gulf with and without eddy. Significant TL changes are observed at certain depths and ranges. It can be seen from Fig. 3 that the warm eddy has a divergence effect on energy, which prevents the acoustic energy away from the center of the eddies. As a result, the location of the convergence zone, the depth of reversal (the depth where acoustic propagation energy is reversed into another direction), and the energy propagation path change a lot with the existence of eddies compared with the background environment. At the range of 245 km, the upper reversal point drops by 240 m due to the eddy effect, which is the main influence of the eddy. Overall, the upper reversal depth increases when approaching the center of the eddy and then slowly decreases. The convergence width and location vary in different convergence zones. In the first convergence zone, the location and width do not change much as a result of the small sound speed disturbance caused by eddy with 50 km. However, from the 2nd to the 11th convergence zones, there is a more significant change, which can be divided into two parts. In terms of eddy existence, the positions of the 2nd to 5th convergence zones move backward. For example, the third and fourth convergence zones move towards the back to 12 km. In terms of the location of 6th–11th, convergence zones bring forward up to 13 km. In addition, the convergence widths generally increase due to the divergence effects of warm eddy. The 5th convergence zone is an exception. The maximum convergence width reaches 25 km, which is more than 10 km than that of the no-eddy environment. Because of the warm eddy, the third lower reversal avoids hitting the bottom, but shows a stronger interaction with bottom at 170 km. The corresponding convergence structure changes after the fifth reversal.

Table 1. Geoacoustic parameters for acoustic propagation modeling.

Sediment depth/m	Sediment type	Density/(g/cm^3)	P-wave speed/(m/s)	P-wave attenuation/(dB/λ)	S-wave speed/(m/s)	S-wave attenuation/(dB/λ)
0–20		1.44	1515	0.33		
20–50		1.7	1670	0.82		
50–200	silt	1.7	1750	1.07	150	0.22
200–600		1.87	1970	1.48		
>600		2.04	2260	1.82		

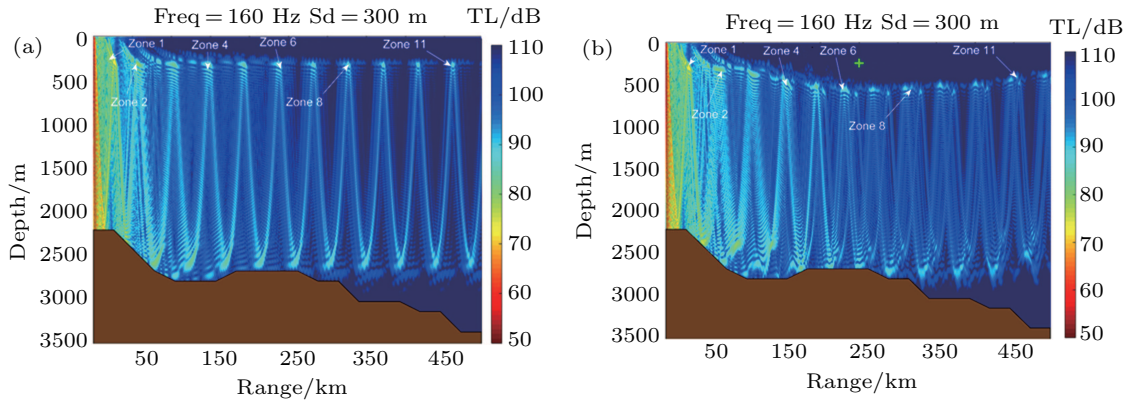


Fig. 3. The comparison of the transmission losses for the environments with/without eddy, with the source depth (Sd) at 300 m and the frequency (Freq) at 160 Hz. The labels "zone n" represents the number of convergence zone for (a) without eddy and (b) with the presence of a warm eddy. The green cross indicates the location of eddy center.

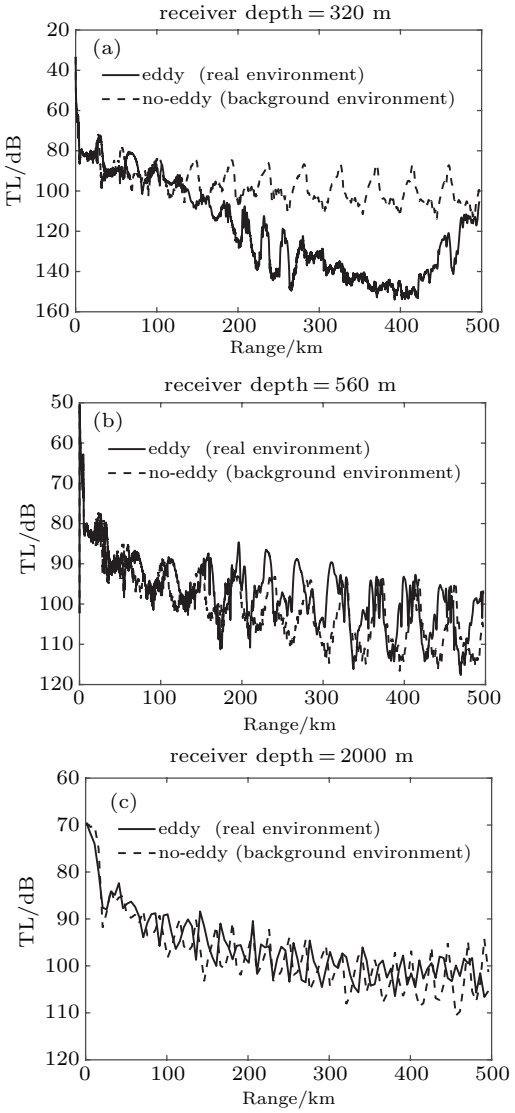


Fig. 4. Transmission losses at three receiver depths: (a) 320 m, (b) 560 m, and (c) 2000 m.

Figure 4 compares the TLs at three different depths of 320 m, 560 m, and 2000 m. It is found that the TL at the depth of 320 m has the biggest change, followed by the depth of 560 m. The bending of the propagation path caused by warm eddies leads to a larger shadow zone in the upper layer. Compared with the condition without eddy, the depth of the shadow zone gradually increases from 300 m in 55 km to 240 m in 245 km, and resumes after going through the eddy center. The differences of TL for two cases at the depth of 560 m reach 10 dB at their corresponding peaks. Figure 4(c) shows that TL is only the overall offset disturbance at the large depth, while the mean value does not change too much. The influence of eddy on TL at the depth of 2000 m is very small. In conclusion, the influence of this warm eddy on the acoustic field is mainly manifest in the area adjacent to the eddy center.

3.1. Normal mode interpretation

To further understand the physical mechanisms causing the acoustic energy fluctuation shown in Fig. 3, the total depth-integrated energy of different normal modes is analyzed hereafter. Furthermore, the change of the overall distribution of total depth-integrated energy amongst modes due to the presence of the eddy is examined hereafter. According to the normal mode theory,[22] the sound field can be expressed as

$$p(r,z) = \frac{\mathrm{i}}{4\rho(z_\mathrm{s})} \sum_{m=1}^{\infty} \varphi_m(z_\mathrm{s})\varphi_m(z) H_0^1(k_{rm} r), \tag{3}$$

where ρ is the density, $p(r,z)$ is the acoustic pressure, $\varphi_m(z)$ is the eigenfunction of mode m, k_{rm} is the eigenvalue, and z_s is the source depth. If the received acoustic pressure at range r_0 is integrated in the depth, then one obtains

$$\begin{aligned} &\int_0^D p(r_0,z)\varphi_l(z)\mathrm{d}z \\ &= \int_0^D \frac{\mathrm{i}}{4\rho(z_\mathrm{s})} \sum_{m=1}^{\infty} \varphi_m(z_\mathrm{s}) H_0^1(k_{r_0 m} r_0)\varphi_m(z)\varphi_l(z)\mathrm{d}z. \end{aligned} \tag{4}$$

Assuming that $\rho(z)$ is a constant, equation (4) becomes

$$\begin{aligned} &\int_0^D p(r_0,z)\varphi_l(z)\mathrm{d}z \\ &= \frac{\mathrm{i}\rho(z)}{4\rho(z_\mathrm{s})} \sum_{m=1}^{\infty} \varphi_m(z_\mathrm{s}) H_0^1(k_{r_0 m} r_0) \int_0^D \frac{\varphi_m(z)\varphi_l(z)}{\rho(z)}\mathrm{d}z. \end{aligned} \tag{5}$$

Since the normal modes are orthogonal[23]

$$\begin{aligned} &\int_0^D \frac{\varphi_m(z)\varphi_l(z)}{\rho(z)}\mathrm{d}z = 0, \quad \text{for } m \neq l, \\ &\int_0^D \frac{\varphi_m^2(z)}{\rho(z)}\mathrm{d}z = 1, \quad \text{for } m = l. \end{aligned} \tag{6}$$

Finally, we obtain

$$\int_0^D p(r_0,z)\varphi_l(z)\mathrm{d}z = \frac{\mathrm{i}\rho(z)}{4\rho(z_\mathrm{s})} \varphi_l(z_\mathrm{s}) H_0^1(k_{r_0 l} r_0). \tag{7}$$

The transmission loss can be obtained by $-10\log I$, where I is the total depth-integrated intensity of different modes defined by

$$I(r_0,z) = \left| \int_0^D p(r_0,z)\varphi_l(z)\mathrm{d}z \right|^2. \tag{8}$$

In this part, the acoustic pressure is calculated by RAM-PE.[19,20] The local normal-mode eigen-functions are obtained from Kraken using the ocean environments at the local range.[24]

Figure 5 shows the integrated energy across depth of different normal modes for the environments with and without eddy, at four different ranges: 26.2 km, 78.5 km, 261.8 km, and 497.3 km, respectively. It can be seen that the energy is mainly in the 48th–106th modes for two cases, while 1st–47th modes and the modes larger than the 107th mode take up little energy at long distances. These three groups of modes correspond to waterborne modes, bottom bounce modes, and leaky

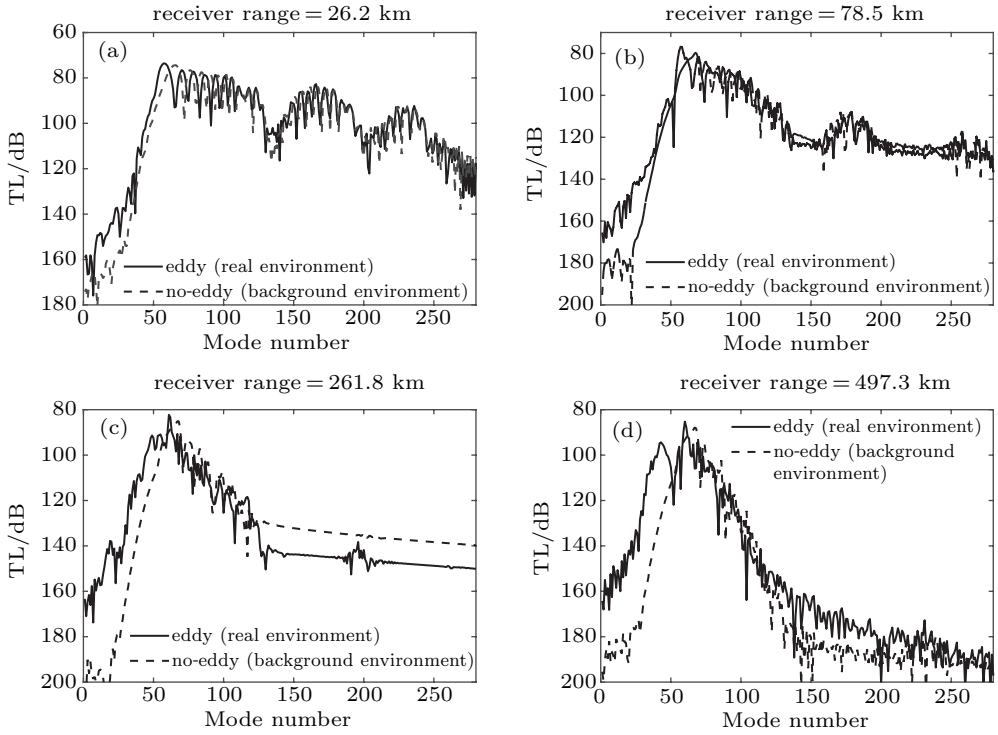


Fig. 5. Comparison of the transmission loss for different modes in the environments with/without eddy at four different ranges: (a) 26.2 km, (b) 78.530 km, (c) 261.8 km, and (d) 497.3 km.

modes. For the source at the depth of 300 m, the waterborne modes carry little at the range of 26.2 km and 78.5 km. Although the leaky modes at the range of 26.2 km carry some energy, it is attenuated quickly as the range increases. Moreover, as the energy disperses causing by the warm eddy, the maximum energy carried by the single mode is reduced.

Furthermore, due to the influence of the warm eddy, the energy contained in higher normal modes gets redistributed into the lower modes. In the range of 26.2 km, the influence of the eddy on the sound speed is relatively small, hence a relatively small acoustic field fluctuation in energy of modes. As the range value approaches the center of eddies, the influence on acoustic propagation becomes more obvious. That, in turn, leads to the redistribution of the energy. Meanwhile, as bathymetry increases, the energy occupied by the waterborne mode increases. For instance, at the range of 497.3 km, the waterborne mode takes up a certain amount of energy and the structure of energy reaches a steady state. As a result, the energy integrated along with the depth is dominated by the bottom bounce modes and waterborne modes at longer ranges such as 261.8 km and 497.3 km. However, although the energy is biased toward the smaller modes, the bottom bounce modes still dominate.

To explain the energy deflection caused by the eddy shown in Fig. 3(b), a single normal mode is used as the initial field for the RAM-PE[21] instead of the standard point source approximation. Specifically, the normalized initial field at the initial position can be obtained from Eq. (3) by Kraken. Then, the acoustic field in the whole computational domain can be determined by recursion using Eqs. (1) and (2) of RAM-PE model. Consequently, the coupling characteristics and energy change paths of different normal modes under eddy environment can be easily analyzed.

To show the influence of warm eddy on the energy path of sound propagation, the field from normal modes 42 and 57 serves as the initial field. The TLs for two different environments with/without eddy are given in Fig. 6.

Figures 6(a) and 6(b) correspond to mode 42. This waterborne mode does not touch the seabed in the whole propagation range. Thus, it can be seen that the propagation path does not change in the environment without eddy. This means that there is no mode coupling occurring. As Fig. 7(a) presents, mode 42 remains the same as that at the range of 261.8 km. However, figure 6(b) illustrates that the energy propagation path changes a lot due to the warm eddies. That is because the warm eddy transmits this mode energy coupling to other modes. These modes are then superimposed on each other to produce an interference structure. The change of the propagation energy trajectory is similar to the TL shadow zone in Fig. 3(b). The depth of the first and the last peak points which corresponds to mode 42 at a range of 0 km is 393.5 m and 2076 m, respectively. In contrast, the values at the range of 261.8 km become 650 m and 2310 m. Due to the influence of the warm eddy, the upper depth boundary of mode 42 increases by 257 m, and the vertical scale covered by this mode is compressed. As the range keeps increasing after going through the center of the eddy, the energy gradually spreads out and returns to the original depth. The offset of the normal wave

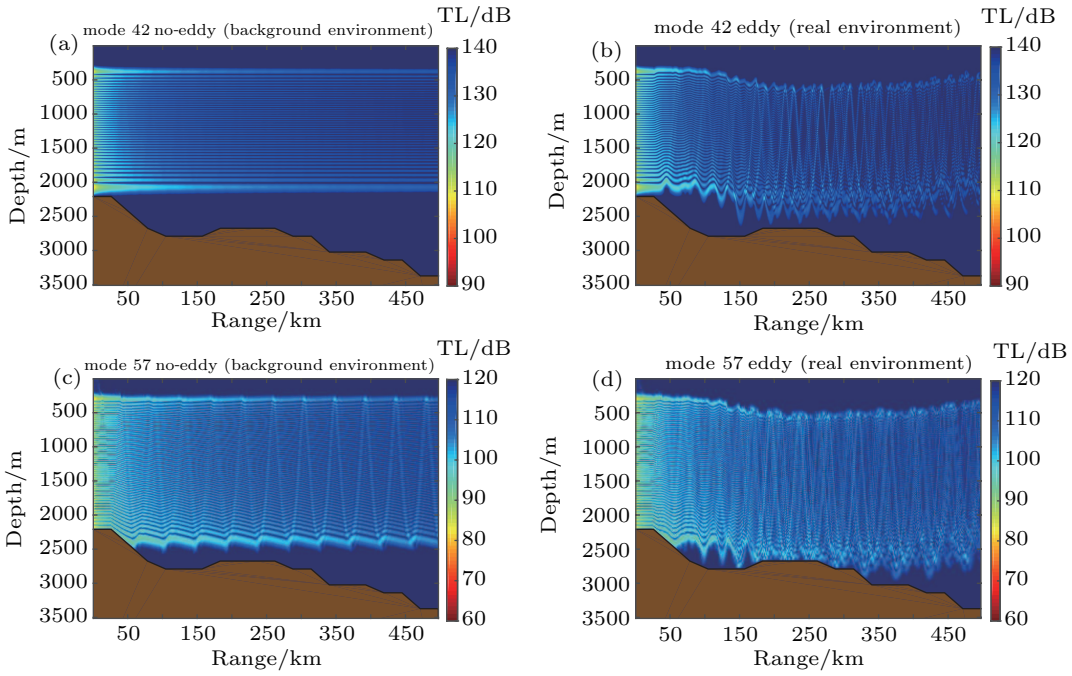


Fig. 6. Comparison of TLs for environments with/without eddy with the initial field of single mode. (a) Waterborne mode 42 in an environment without eddy, (b) mode 42 in an environment with eddy, (c) bottom-bounce mode 57 in an environment without eddy, and (d) mode 57 in an environment with eddy.

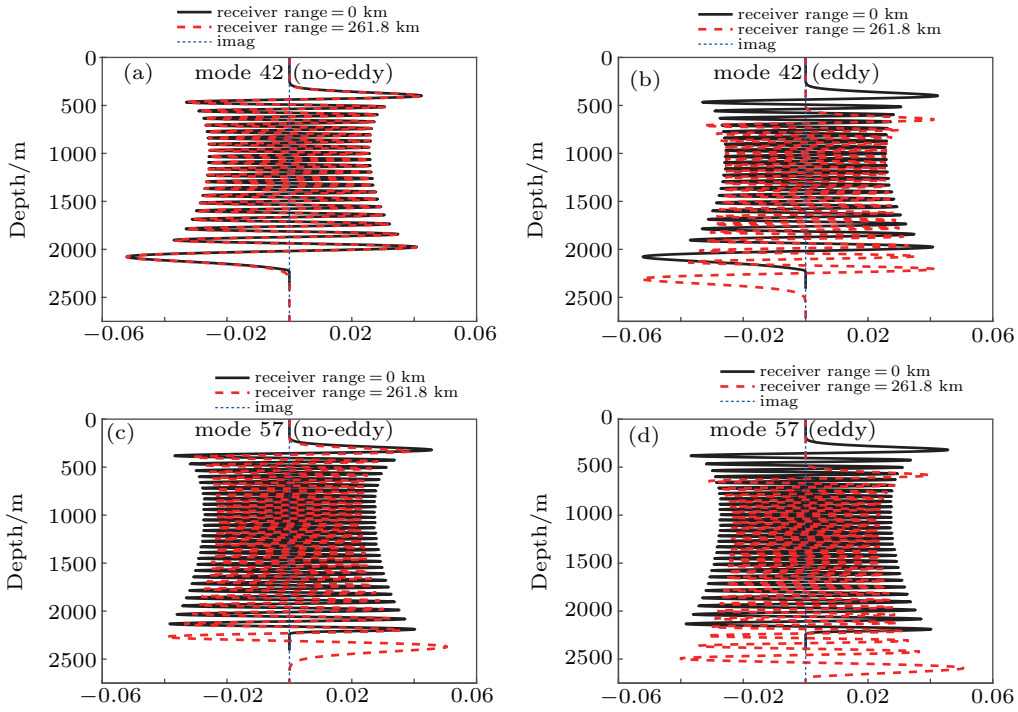


Fig. 7. Comparison of the normal mode eigen-functions for environments with/without eddy. (a) Mode 42 in an environment without eddy, (b) mode 42 in an environment with eddy, (c) mode 57 in an environment without eddy, and (d) mode 57 in an environment with eddy.

in Fig. 6(b) at eddy center is consistent with that of Fig. 7(b), where energy is redistributed at 261.8 km.

In contrast, figures 6(c) and 6(d) correspond to mode 57, which is a bottom bounce mode at the original range and interacts with the bottom. Even though the sound speed in Fig. 6(c) does not change at the same depth, the change of bathymetry leads to the mode coupling at the range from 26 km to 50 km. Thus, some waterborne modes obtain certain energy. This is the main reason why the energy shifts downward at the range from 26 km to 50 km. Figure 7(c) also shows the bottom effect for the vertical scale and the last peaks of those modes. When the effects of the seabed topography couple with the eddy, the sound propagation path becomes extremely complex. The mode coupling causing by the warm eddy makes the propagation path interact with the seafloor again at the range from 150 km to 300 km. Both figures 6(d) and 7(d) confirm that the

existence of eddies prompts the energy shift downward and the mode coupling, which constitutes the main influential mechanism of the eddy on sound propagation.

3.2. Ray theory interpretation

As stated in Ref. [23], the normal mode has a corresponding relation with the ray path, so the ray calculated by Bellhop[25] can also be used to illustrate the change in the acoustic propagation path. Since the energy occupied by waterborne modes and leaky modes at a long distance is small, figure 8 focuses instead on the ray path associated with bottom bounce modes which carry more energy. If there is no effect, then the blue line in Fig. 8 will directly hit the seafloor three times, then a stable curved structure is formed. Compared with the blue line (no eddy case), it is obvious that the red ray bends down first, then lifts because of the warm eddy. However, the rays touch the bottom once again at range 150 km–300 km. This is because of the strong sound speed fluctuation near the center range of the eddy. The width and location of the convergence zone and the reversal depth are also changed. It is consistent with the normal mode analysis above.

The warm eddy has a diverging effect on energy, as shown in Fig. 3(b). The divergence effect is explored via the arrival angle of the receiving ray, which is computed with the Bellhop model. The arrival angle at different receiver depths for environments with and without eddy within the range of 500 km is illustrated in Fig. 9. The blue dots represent the arrival angles under the environment without eddy, while the red dots represent the arrival angles in the presence of an eddy. Figures 9(a)–9(c) show the arrival angles at the depths of 320 m, 560 m, and 2000 m, respectively. It can be found that the arrival angles at the depth of 320 m undergo the most noticeable change, followed by 560 m. While the disturbance of arrival angles at the depth of 2000 m is relatively small, the characteristics are similar to those in Fig. 4. The fluctuation of arrival angle at the depth of the eddy center is much larger than other depths. Meanwhile, it can be seen from Fig. 9(a) that there are various angles of arrival rays within 50 km. This happens because the energies of the rays with large arrival angle do not decay. The warm eddy has a weak effect at those ranges, as a result of which, the arrival angles display little difference between the two cases. As the range increases, the arrival

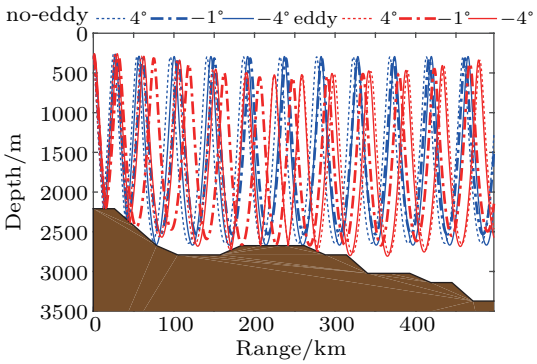


Fig. 8. Comparison of the ray paths for the environments with (red line)/without eddy (blue line).

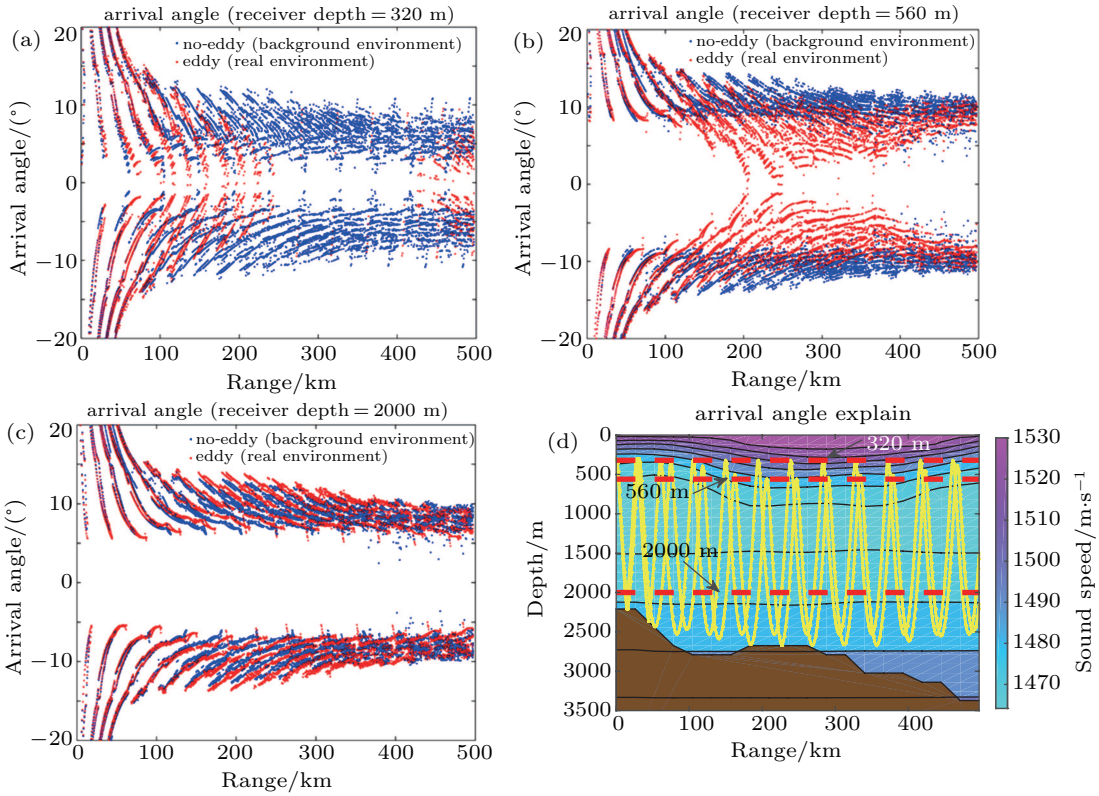


Fig. 9. The arrival angles at three different depths for the environments with and without eddy: (a) 320 m, (b) 560 m, (c) 2000 m, and (d) ray paths.

angle decreases gradually and then stabilizes at a certain stage. This is because there exist only rays that are in line with bottom bounce rays such as those labeled with yellow-dashed line in Fig. 9(d). However, there is a marked difference in the arrival angles with different receiving ranges and depths with the presence of eddy. When the receiver is at the depth of 320 m, the arrival ray decreases sharply until it disappears in the range between 50 km and 300 km due to effects of the warm eddy. There are more small arrival angles occurring in the depth of 560 m, because the energy path bends downward from the upper layer, as shown in Fig. 9(d) with a yellow-solid line. Figure 9(c) illustrates that the arrival angle changes little at depth of 2000 m, which is outside the main effect of the warm eddy. According to Snell's law, the sound speed fluctuation caused by warm eddy leads to the ray leak from the eddy, as shown in Fig. 9(d).

4. Sound field fluctuations caused by the eddy's dynamic

Previous research has been limited to the study of static eddies. However, the acoustic environment in the Gulf of Mexico is complex and dynamic, thus affecting the acoustic field dynamically. In terms of the temporal evolution of its shapes and the change rate of the temperature, the warm eddy in this section is roughly divided into time interval, eddy generating (August 4, 2014–August 19, 2014), eddy maturing (August 20, 2014–October 12, 2014), and eddy terminating (October 13, 2014–October 29, 2014). The formation and extinction features throughout the eddy's evolving process are confirmed by the change of the shape of the eddy,[26] as determined by the eddy tracking method described in Section 2. As seen from Fig. 10(a), the radius of the eddy increases during the first 1/5 (eddy generating) of the entire lifespan from August 4, 2014 to October 29, 2014, remains stable at the next 3/5 (eddy maturing), and declines rapidly at the last 1/5 (eddy terminating). Meanwhile, the location of the eddy center also varies some. Figure 10(b) shows the contour fluctuation of the sound speed at a different period when the warm eddy exists. It can be seen clearly that the influence of the warm eddy mainly occurs the thermocline depths from 70 m to 1050 m.

The fluctuation of sound field in different periods along the propagation path is examined, as shown by the black-dashed line in Fig. 10(a). The source depth is 300 m. To obtain a smoother and more stable acoustic field, eleven frequency points from 150 Hz to 170 Hz are used. As shown in Fig. 11, the results are presented at four different receiving distances. It can be seen that the acoustic energy disturbance reaches more than 30 dB at the same ranges under different environmental disturbances generated in different periods of the eddy.

The maximum fluctuation of sound field significantly depends on the receiving distance. It can be found that the energy at the range of 497.3 km has the biggest change during the eddy's lifespan, followed by 261.8 km, while it will be much smaller at 26.2 km. Although at different receiving distances, the maximum fluctuation of acoustic field varies significantly, there are some similarities. The energy demonstrates rich variety before and after October 2. The energy disturbance caused by the change of the warm eddy is oscillating and will not exceed 15 dB before that day. However, the received energy has sharply decreased ever since.

As shown in Fig. 12(a), the sound speed has changed little and slowly at the generating period, so the acoustic field can remain relatively stable before August 19, 2014. During the maturing period, the warm eddy has a strong influence on the sound speed; meanwhile, the eddy is moving westward as a whole. The moving eddy causes the sound field to oscillate from August 20 to October 2. Figure 12(b) typically shows the influence of the eddy on propagation path change on September 17th. However, as the eddy keeps moving westward, the relative location between the source and eddy center becomes closer.

Although the eddy remains stable, the acoustic energy is

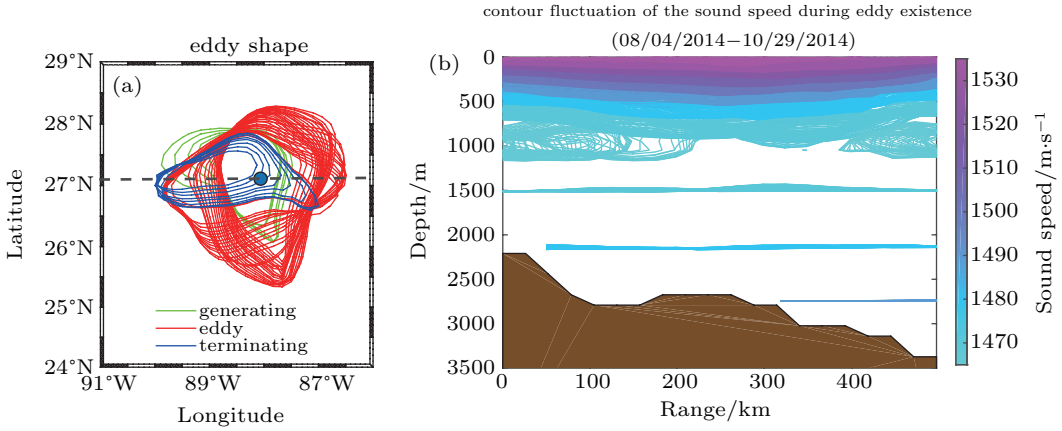


Fig. 10. Example of eddy tracking. (a) The eddy shapes at three different time periods. (b) Superimposed contours of sound speed structure obtained during the whole existence of the warm eddy.

strongly attenuated by the seabed from October 2 to October 12. As shown in Fig. 12(c), the ray path bends down quickly so that the energy can interact with the bottom more frequently, which causes a strong energy attenuation. This proves that the sound speed contributes greatly to the energy oscillating disturbance, while the relative location of eddy center and source is mainly responsible for energy propagation path change so that the acoustic energy can be strongly attenuated by the seabed. Although the acoustic energy remains highly attenuated because of the mutual interaction between the ray and the seabed, the eddy begins to enter the recession period since October 13. This means that the shape and sound speed of eddy change quickly, which causes the energy to reach a more stable value in the terminating period, as presented in Fig. 12(d).

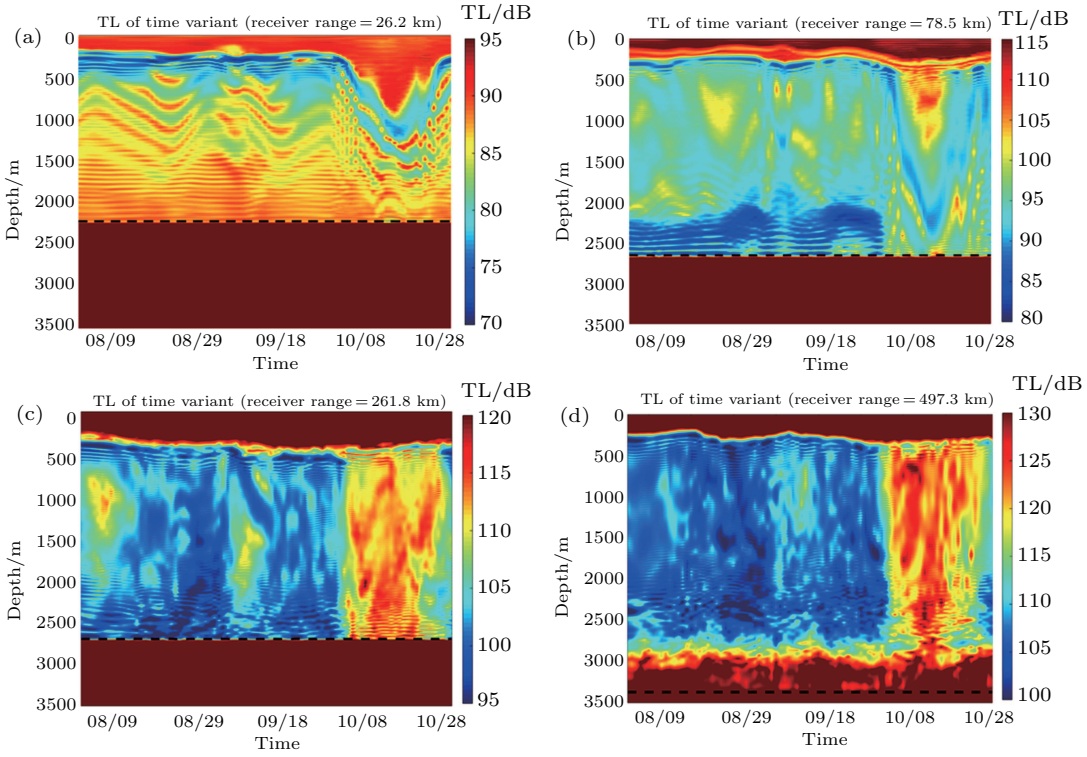


Fig. 11. Fluctuations of the transmission loss vs. depths throughout the whole eddy lifespan at receiving ranges of (a) 26.2 km, (b) 78.5 km, (c) 261.8 km, and (d) 497.3 km.

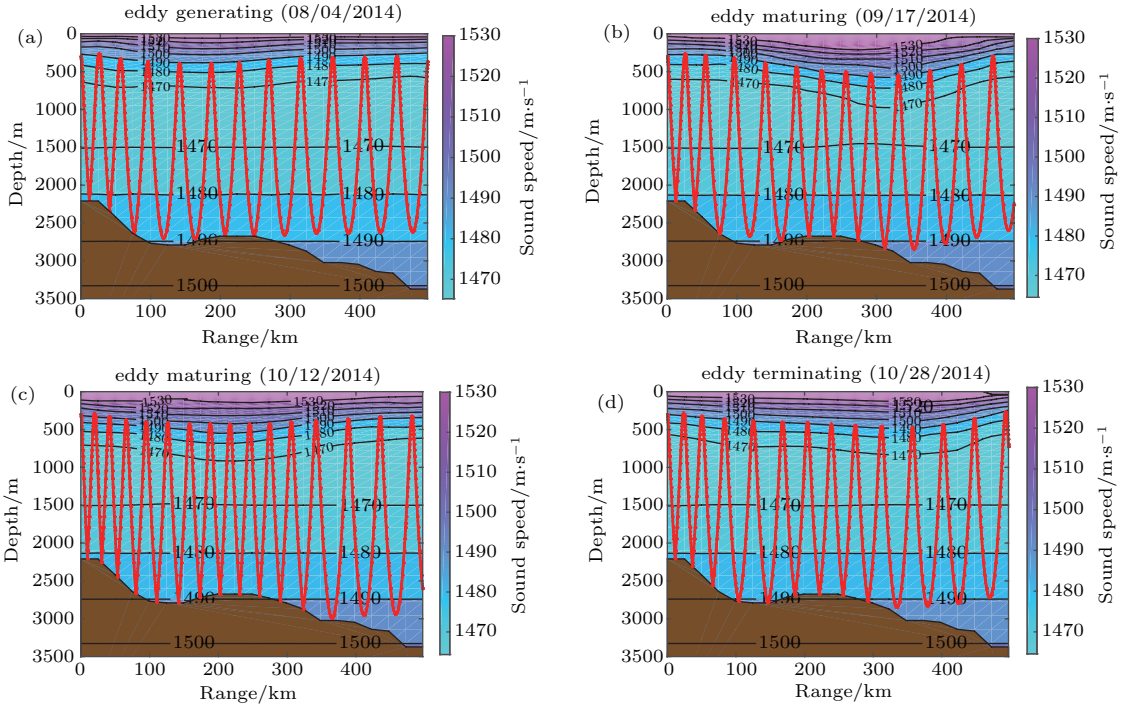


Fig. 12. Sound speed disturbance colormap with sound ray explanation at four different periods of a warm eddy: (a) eddy generation, (b) eddy maturing with small attenuation, (c) eddy maturing with strong attenuation, and (d) eddy terminating.

5. Conclusions and further studies

In this study, an automatic detection method in combination with satellite remote sensing data and CMEMS data is used to identify and track eddies in the Gulf of Mexico. Physical parameters of the eddies, such as lifespan, radius, and distribution position are first examined and used to determine the spatio-temporal evolution of a strong warm eddy separated from the Mexico current. Then, the parabolic equation method is used to comprehensively analyze the influence of this strong warm eddy on sound propagation during its lifespan. Furthermore, the normal mode and ray theories, the total depth-integrated energy and single mode as initial field method, and the receiving arrival angle are all used to explain and understand the effect of warm eddies on acoustic propagation. Based on the methods and models that are used for analysis, the following conclusions have been obtained.

(i) The location of the convergence area, the depth of reversal, and the energy propagation path vary significantly with the existence of eddies compared with background environment. The results show that the warm eddies can disperse the sound energy, change the propagation paths, cause the convergence zone to approach the sound source, and broaden the convergence zone. Moreover, the mode coupling caused by the warm eddy contribute to redistribution amongst normal modes and the change of the acoustic propagation path.

(ii) The effects of the warm eddies on the sound speed, acoustic propagation path, and arrival angle remain active at the scale of eddy existence.

(iii) Throughout the whole of these three periods (eddy generating, eddy maturing, and eddy terminating), the fluctuation in the transmission loss is up to 30 dB and presents different features. The results show that the sound speed fluctuation is a critical factor to cause the energy oscillating disturbance, while the energy propagation path change is mainly triggered by the relative location change between the eddy and source, so that the acoustic energy is strongly attenuated by the seabed.

(iv) The receiving arrival angle is an important parameter in understanding the divergence effect of warm eddies on acoustic propagation.

However, it should be noted that, for the sake of simplicity, the three-dimensional effects caused by mesoscale eddies have not been taken into account in the current study. Further developments may consider this point. In addition, more physical characteristics of mesoscale eddies can be further determined to potentially create more realistic modes for dynamic eddies throughout their lifespan.

Acknowledgment

The authors would like to thank Prof. Jixun Zhou, Ph.D. candidate Nick Durofchalk in Georgia Tech, and Dr. Jun Tang in Harbin Engineering University for their invaluable suggestions and discussions. The authors would also like to thank Prof. Changming Dong and Prof. Sen Wang from Nanjing University of Information Science and Technology for sharing the eddy detection and tracking code.

References

[1] Munk W 2011 *Tellus Ser. A* **63** 190
[2] Zhang Z, Wang W and Qiu B 2014 *Science* **345** 322
[3] Chen G, Hou Y and Chu X 2011 *J. Geophys. Res. Oceans* **116** C06018
[4] Chelton D B, Schlax M G and Samelson R M 2011 *Prog. Oceanography* **91** 167
[5] Shang E C 1989 *J. Acoust. Soc. Am.* **85** 1531
[6] Henrick R F, Siegmann W L and Jacobson M J 1977 *J. Acoust. Soc. Am.* **61** 860
[7] Henrick R F, Jacobson M J and Siegmann W L 1980 *J. Acoust. Soc. Am.* **67** 121
[8] Hall M V and Irving M A 1989 *J. Acoust. Soc. Am.* **86** 1465
[9] Vastano A C and Owens G E 1973 *J. Phys. Oceanography* **3** 470
[10] Weinberg N L and Zabalgogeazcoa X 1977 *J. Acoust. Soc. Am.* **62** 888
[11] Baer R N 1981 *J. Acoust. Soc. Am.* **69** 70
[12] Lawrence M W 1983 *J. Acoust. Soc. Am.* **73** 474
[13] Munk W H 1980 *J. Phys. Oceanography* **10** 596
[14] Chen C, Yang K D, Ma Y L and Duan R 2016 *Chin. Phys. Lett.* **33** 104302
[15] Heaney K D and Campbell R L 2016 *J. Acoust. Soc. Am.* **139** 918
[16] Dong C, Nencioli F, Yu L and Mcwilliams J C 2011 *IEEE Geosci. Remote Sens. Lett.* **8** 1055
[17] von Schuckmann K, Le Traon P Y, Alvarez-Fanjul E, Axell L, Balmaseda M, Breivik L A, Brewin R J W, Bricaud C, Drevillon M and Drillet Y 2016 *J. Oper. Oceanogr.* **9** s235
[18] Ferry N, Parent L, Masina S, Storto A, Haines K, Valdivieso M, Barnier B, Molines J, Zuo H and Balmaseda M *CMEMS Version Scope: Version 1*
[19] Zeddies D, Denes S, Pyć C and Spring S 2017 *Contract* **2017** 111331
[20] Collins M D 1992 *J. Acoust. Soc. Am.* **92** 2069
[21] Collins M D 1993 *J. Acoust. Soc. Am.* **93** 1736
[22] Jensen F B 1993 *Acoustic Signal Processing for Ocean Exploration* (Moura J M F and Lourtie I M G, Ed.) (Dordrecht: Springer) pp. 3–20
[23] Jensen F B, Kuperman W A, Porter M B and Schmidt H 2011 *Computational Ocean Acoustics* (New York: Springer)
[24] Porter M B 1992 *the KRAKEN Normal Mode Program, Report*
[25] Porter M B and Bucker H P 1987 *J. Acoust. Soc. Am.* **82** 1349
[26] Dong C 2016 *Oceanic Eddy Detection and Analysis* (Beijing: Science Press) pp. 94–97 (in Chinese)